works of these materials by direct synthesis. In the as-synthesized precursors of CoAPO-5 and -11, Co(II) cations substitute for the Al(III) framework cations thereby forming $Co^{II}O_4$ tetrahedra, the frameworks becoming negatively charged. In the CoAPO-21 precursor, the incorporated Co(II) occupy both four-coordinated and five-coordinated sites. After calcination in O_2 at elevated temperatures, some of the Co(II) cations are oxidized and remain in the frameworks as $Co^{III}O_4$ tetrahedra along with some unoxidized $Co^{II}O_4$ tetrahedra; the rest are driven out of and become chemically anchored onto the frameworks as $Co^{II}O_6$ octahedra. The tetrahedral $Co^{III}O_4$ species in CoAPO-5 can be readily but not completely reduced back to $Co^{II}O_4$ tetrahedra; but those in CoAPO-11 and CoAPO-25 are difficult to reduce. Since the reduction of each framework Co(III) to Co(II) introduces a proton to balance the negatively charged framework, the acidity of CoAPO-5 is greatly improved compared with that of the parent ALPO-5. CoAPO-11 and CoAPO-25, on the other hand, are not superior to their aluminophosphate analogues in acidity. CoAPO-5 is very active for methanol conversion to hydrocarbons, the predominant product being propene. The majority of the methanol conversion product on both CoAPO-11 and CoAPO-25 is dimethyl ether.

Acknowledgment. We thank SERC for general support and Unilever Plc for financial support to J.C. We are also indebted to R.H. Jones, P.A. Wright, and S. Natarajan for helpful suggestions and discussion.

Registry No. H_2O, 7732-18-5; N_2, 7727-37-9; MeOH, 67-56-1.

Photooxidation of Hexacarbonylmolybdenum(0) in Sodium Zeolite Y to Yield Redox-Interconvertible Molybdenum(VI) Oxide and Molybdenum(IV) Oxide Monomers

Saim Özkar

Chemistry Department, Middle East Technical University, 06531 Ankara, Turkey

Geoffrey A. Ozin* and Richard A. Prokopowicz

Lash Miller Chemical Laboratories, Advanced Zeolite Materials Science Group, University of Toronto, 80 St. George Street, Toronto, Ontario, Canada M5S 1A1

Received May 27, 1992. Revised Manuscript Received August 12, 1992

An analysis of the photooxidation reaction of α-cage located, site II sodium cation anchored *trans*-(ZONa)···(OC)$Mo(CO)_4$(CO)···(NaOZ) exposed to O_2 in sodium zeolite Y ($Na_{56}Y$) has been carried out using various techniques (PXRD, EXAFS, MAS/DOR-NMR, EPR, XPS, UV–vis, FTIR, gravimetry). The results have shown that it cleanly and qunatitatively converts to molybdenum(VI) oxide and CO_2 as the sole reaction products according to

$$n[Mo(CO)_6]\text{–}Na_{56}Y + {}^9/_2 nO_2 \xrightarrow{h\nu} n[MoO_3]\text{–}Na_{56}Y + 6nCO_2$$

over the full loading range $0 < n \leq 16$. Vacuum, thermally induced reductive elimination of O_2 from the molybdenum(VI) oxide photoproduct is quantitative at 400 °C and yields molybdenum(IV) oxide with no evidence for any other products having oxygen stoichiometries differing from two and three. This reduction process can be quantitatively reversed by exposure of the molybdenum(IV) oxide product to O_2 at 400 °C, according to

$$n[MoO_3]\text{–}Na_{56}Y \underset{400\ °C}{\overset{400\ °C,\ \text{vacuum}}{\rightleftharpoons}} n[MoO_2]\text{–}Na_{56}Y + {}^1/_2 nO_2$$

The structural and spectroscopic analyses demonstrate that over the loading range $0 < n \leq 16$, the aforementioned molybdenum oxides are located in the α-cages of $Na_{56}Y$ as redox-interconvertible monomers denoted (ZO)···MoO_3···(NaOZ) and (ZO)···MoO_2···(NaOZ), where ZO represents an oxygen framework six-ring or four-ring "primary" anchoring interaction and NaOZ represents a site II or site III sodium cation "secondary" interaction (the latter involving the oxygen atom of an oxomolybdenum bond). A comparison of the results for the related molybdenum and tungsten systems reveals some interesting and important similarities and differences, which are considered in terms of potential catalytic, solid-state, and materials chemistry applications envisioned for these novel kinds of molecular metal oxide nanocomposites.

Introduction

It is well-known that many molybdenum and tungsten compounds are similar in terms of their stoichiometries, structures, and chemical properties. However, there are examples of analogous compounds whose differences in properties are sometimes surprising and often difficult to explain.[1] The photooxidation of hexacarbonylmolybdenum(0) and hexacarbonyltungsten(0) contained in sodium zeolite Y turns out to be a case in point and definitely falls into this "unexpected" category. Details of the $n[W(CO)_6]\text{–}Na_{56}Y/O_2/h\nu$ system have been reported by us previously;[2-4] the analogous $n[Mo(CO)_6]\text{–}Na_{56}Y/$

* To whom correspondence should be sent.

(1) Cotton, F. A., Wilkinson, G., *Advanced Inorganic Chemistry*, 5th ed.; Wiley: New York, 1988.

0897-4756/92/2804-1380$03.00/0

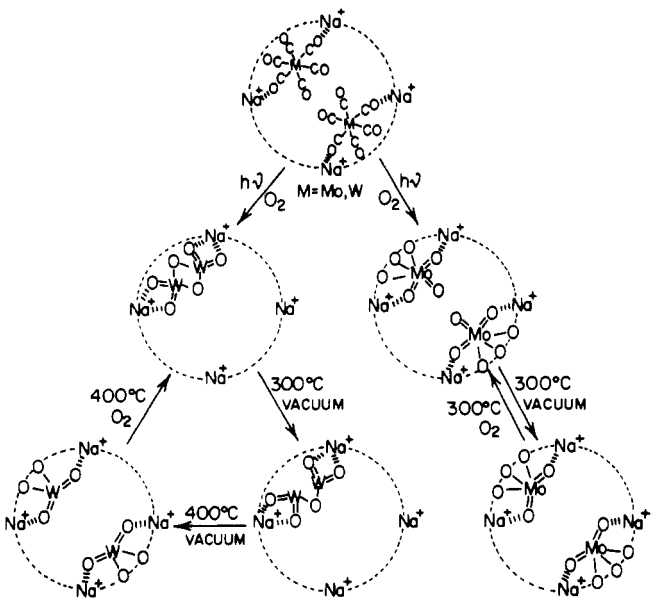

Figure 1. Photooxidation chemistry of precursor 16[M-$(CO)_6$]-$Na_{56}Y$ and thermal reversible redox chemistry of product 16[MoO_3]-$Na_{56}Y$ for M = Mo, W.

$O_2/h\nu$ system is new and forms the subject of the present study.

Let us briefly review pertinent features of the intrazeolite photooxidation of zeolite Y encapsulated $W(CO)_6$ by O_2. The process is clean and quantitative and is described[2] by the reaction stoichiometry

$$n[W(CO)_6]\text{-}Na_{56}Y + {}^9/_2 nO_2 \xrightarrow{h\nu} n[WO_3]\text{-}Na_{56}Y + 6nCO_2$$

which can be achieved in a single impregnation photooxidation step. The above stoichiometry is applicable over the full loading range $0 < n \leq 16$, where 16[$W(CO)_6$]-$Na_{56}Y$ represents saturation adsorption corresponding to 2[$W(CO)_6$] per α-cage. The precursor[3] has been structurally defined as *trans*-$(ZONa_{II})\cdots(OC)W(CO)_4(CO)\cdots(Na_{II}OZ)$, and the photooxidation product as $(ZONa_{II})\cdots O_2W(\mu\text{-}O)_2WO_2\cdots(Na_{II}OZ)$. The $W(CO)_6$ monomer is anchored via cation–carbonyl group interactions, whereas the W_2O_6 dimer is tethered by cation–dioxo group linkages.[4] Both the precursor and product are housed exclusively in the more spacious α-cages, with the dominant cation interactions involving the tetrahedral array of site II Na^+ cations.[4] These proposed features are illustrated in Figure 1.

From consideration of the steric and spatial demands of $W(CO)_6$ relative to W_2O_6, it can be determined that the process of photooxidizing $W(CO)_6$ to W_2O_6 within the α-cage creates space, thereby allowing sequential impregnation/photooxidation steps to be achieved.[2] In the special circumstance of repetitive saturation–absorption followed by photooxidation steps, one can approach a maximally loaded photoproduct composition of 32[WO_3]-$Na_{56}Y$ as illustrated in the following scheme:[2]

$$16W(CO)_6\text{-}Na_{56}Y \rightarrow 16WO_3\text{-}Na_{56}Y$$
$$8W(CO)_6,\ 16WO_3\text{-}Na_{56}Y \rightarrow 24WO_3\text{-}Na_{56}Y$$
$$4W(CO)_6,\ 24WO_3\text{-}Na_{56}Y \rightarrow 28WO_3\text{-}Na_{56}Y$$
$$\vdots$$
$$1W(CO)_6,\ 31WO_3\text{-}Na_{56}Y \rightarrow 32WO_3\text{-}Na_{56}Y$$

A combination of spectroscopy, diffraction, and microscopy[2-4] have demonstrated that the W_2O_6 dimer structure is maintained across the full loading range $0 < n \leq 32$. The half-loaded sample $n = 16$ is described as a supralattice of dimers 8[W_2O_6]-$Na_{56}Y$, whereas the completely filled sample $n = 32$ is a supralattice of dimers-of-dimers 16[W_2O_6]-$Na_{56}Y$. Chem-X molecular graphics representations of these two structures have been previously reported.[3] That study showed that the two dimers jointly occupying each α-cage in 16[W_2O_6]-$Na_{56}Y$ are configured orthogonal to each other. An especially fascinating property of these W_2O_6 dimers is their intrazeolite redox chemistry.[4] Vacuum thermal treatment results in clean reductive-elimination of O_2 in what appears to be two distinct steps. These occur around 300 and 400 °C according to the following reaction stoichiometry:

$$n[WO_3]\text{-}Na_{56}Y \xrightarrow[\text{vacuum}]{300\ ^\circ C} n[WO_{2.5}]\text{-}Na_{56}Y \xrightarrow[\text{vacuum}]{400\ ^\circ C} n[WO_2]\text{-}Na_{56}Y$$
$$n[WO_2]\text{-}Na_{56}Y \xrightarrow[O_2]{300\ ^\circ C} n[WO_3]\text{-}Na_{56}Y$$

With increasing loading, the n[WO_3]-$Na_{56}Y$ parent compound changes in color from white to light grey, the n[$WO_{2.5}$]-$Na_{56}Y$ intermediate changes from metallic blue to metallic grey, and the n[WO_2]-$Na_{56}Y$ final product changes from white to light grey. The latter material can be cleanly and quantitatively reoxidized at 300 °C in O_2 back to the starting material, but without any evidence of producing the intermediate shown above. A multiple technique analysis[4] applied to the intermediate and final products in this system has elucidated certain key aspects relating to their structure, bonding and electronic properties. At $n = 16$, the intermediate contains a supralattice of *single* oxo-bridged dimers $(ZONa)\cdots O_2W(\mu\text{-}O)WO_2\cdots(NaOZ)$ and the final product, a supralattice of monomers $(ZO)\cdots WO_2\cdots(NaOZ)$. At $n = 32$, the intermediate contains a supralattice of tetramers $(ZONa)\cdots O_4W_2(\mu\text{-}O)_2W_2O_4\cdots(NaOZ)$, while the final product retains a supralattice of monomers $(ZO)\cdots WO_2\cdots(NaOZ)$. All of these compounds appear to be diamagnetic, spin-paired (EPR silent, NMR active) materials.[4] It has been shown[4] that n[WO_2]-$Na_{56}Y$ unequivocally contains W^{4+}, and n[$WO_{2.5}$]-$Na_{56}Y$ is best described as containing all W^{5+}/W^{5+} centers rather than mixed-valence W^{4+}–W^{6+} sites.

While 16[$W(CO)_6$]-$Na_{56}Y$ and 16[$Mo(CO)_6$]-$Na_{56}Y$ are similar in terms of their α-cage adsorption, structure, and cation anchoring properties,[2,3] they turn out to be quite different with respect to their photo-oxidation chemistry. In this study, it is shown that the sole photoproduct over the loading range $0 < n \leq 16$ is monomeric $(ZO)\cdots MoO_3\cdots(NaOZ)$. Vacuum thermal treatment of the zeolite encapsulated molybdenum(VI) oxide monomers at 400 °C cleanly transforms them to molybdenum(IV) oxide monomers $(ZO)\cdots MoO_2\cdots(NaOZ)$. This process can be quantitatively reversed at 400 °C in O_2. No other oxides of molybdenum were observed to participate in these redox reactions. Thus, the reaction stoichiometry can be written

$$n[MoO_3]\text{-}Na_{56}Y \underset{400\ ^\circ C}{\overset{400\ ^\circ C,\ \text{vacuum}}{\rightleftharpoons}} n[MoO_2]\text{-}Na_{56}Y + {}^1/_2 nO_2$$

(2) Ozin, G. A.; Özkar, S. *J. Phys. Chem.* **1990**, *94*, 7556. Ozin, G. A.; Özkar, S., Macdonald, P. M. *J. Phys. Chem.* **1990**, *94*, 6939. Ozin, G. A.; Kirkby, S.; Meszaros, M.; Özkar, S.; Stein, A.; Stucky, G. D. Intrazeolite Semiconductor Quantum Dots and Quantum Supralattices. In *Materials for Nonlinear Optics*; p. 554, ACS Symp. Ser. No. 455; American Chemical Society: Washington, DC, 1990. Ozin, G. A.; Özkar, S. *Adv. Mater.* **1992**, *4*, 11.

(3) Ozin, G. A.; Özkar, S.; Moller, K.; Bein, T. *J. Am. Chem. Soc.* **1991**, *112*, 9575. Moller, K.; Bein, T.; Özkar, S.; Ozin, G. A. *J. Phys. Chem.* **1991**, *95*, 5276.

(4) Ozin, G. A.; Malek, A.; Prokopowicz, R. A.; Macdonald, P. M.; Özkar, S.; Moller, K.; Bein, T.; *Mater. Res. Soc. Symp. Ser.* **1991**, *233*, 109. Özkar, S.; Ozin, G. A.; Prokopowicz, R. A. *J. Am. Chem. Soc.*, in press.

The following describes for the first time, full details of a multiple technique analysis of the photooxidation reaction of $n[Mo(CO)_6]$–$Na_{56}Y$ to $n[MoO_3]$–$Na_{56}Y$, and the thermally induced reversible redox process involving $n[MoO_3]$–$Na_{56}Y$ and $n[MoO_2]$–$Na_{56}Y$.

Experimental Section

The high-purity, crystalline sodium zeolite Y, having the unit cell composition $Na_{56}(AlO_2)_{56}(SiO_2)_{136}\cdot xH_2O$ was obtained from Dr. Edith Flanigen at UOP, Tarrytown, NY. To remove cation defect sites, thermally dehydrated/calcined $Na_{56}Y$ was slurried with a 0.01 M NaCl, 0.01 M NaOH solution and washed until free of Cl^-. This procedure results in a material which contains neither OH_α nor OH_β groups at levels detectable by mid-IR. $(NH_4)_{56}Y$ and $H_{56}Y$ were prepared by the use of standard ion exchange techniques and deammination procedures.[5] All of the zeolite samples were stored over saturated NH_4Cl solution to ensure constant humidity until use. The $Mo(CO)_6$ was purchased from Strem Chemicals Inc., Newbury-Port, MA.

The precursor samples denoted $n[Mo(CO)_6]$–$Na_{56}Y$ and the photooxidation products denoted $n[MoO_3]$–$Na_{56}Y$ were prepared according to the procedures[2,3] described previously, using specially designed cells[6] for complete in situ treatments. The thermal reductive–elimination and oxidative–addition of oxygen, for the interconversion of $n[MoO_3]$–$Na_{56}Y$ and $n[MoO_2]$–$Na_{56}Y$, were carried out in the cells at 400 °C, under vacuum and in 600 Torr of O_2 respectively.

The gravimetric analyses were performed in a specially designed cell consisting of a quartz tube (25 mm in diameter and 12 cm in length) and a greaseless stopcock, which allowed the hexacarbonylmolydenum(0) precursor to be admitted or a vacuum applied. After in situ dehydration and calcination,[2,3] the zeolite sample was exposed to the hexacarbonylmolybdenum(0) vapor. The increase in mass was determined using an analytical balance. Exposure to the hexacarbonylmolybdenum(0) vapor was continued gradually until no further increase in the mass of the zeolite sample was observed. The sample was then irradiated in the presence of oxygen gas, using a 450-W high-pressure xenon arc lamp (OSRAM XBO), a 10-cm water cell–IR filter, and a $\lambda < 345$ nm optical cutoff filter. After pumping out the gases (O_2 and CO_2) at room temperature, the sample was heated for 3 h at 400 °C under vacuum and then 3 h at 400 °C in the presence of oxygen. The changes in mass were recorded at every stage and used for the stoichiometric determinations.

Elemental analyses for Na, Al, and Mo were performed by Neutron Activation Analysis on the University of Toronto Slowpoke Reactor.

The mid-IR spectra were obtained on a Nicolet 20SXB FTIR spectrometer. All spectra presented have been obtained by subtraction of the spectrum of dehydrated zeolite from that of the hexacarbonylmolybdenum(0)-impregnated sample. Optical reflectance spectra were obtained on a Perkin-Elmer 330 instrument using a $BaSO_4$ disk as a reference. Powder XRD patterns were recorded on a Philips PW 1051 and a Scintag PADX θ–θ diffractometer using Ni-filtered Cu Kα radiation (1.541 78 Å). ^{29}Si, ^{27}Al, and ^{23}Na MAS NMR spectra of solid samples were recorded on a Chemagnetics CMX-300 instrument. ^{23}Na DOR NMR spectra were recorded at a 11.7-T magnetic field on a Chemagnetics CMX-500 spectrometer using a home-built probe.[16] The spinning speeds were 5 kHz (inner rotor) and 600–800 Hz (outer rotor). Solid-state EPR data were collected on a Bruker ESP-300 spectrometer. XPS measurements were performed at the University of Western Ontario Surface Science Facility using an SSX-100 system which utilized monochromatic Al Kα X-rays capable of being focused to a spot size of 150 μm and a pass energy of 50 eV. Binding energies have been corrected for sample charging effects by referencing all peaks to the C(1s) peak corresponding to the adventitious carbon component which was assigned the value[7] of 284.6 eV. Differential charging effects were compensated using a conductive mesh-electron flood gun technique[8] and were thus reduced to yield C(1s) line widths of 1.5 eV at fwhm. Quantitative elemental composition measurements were made by correction of integrated peak intensities using Scofield factors[9] modified to account for the kinetic energy dependence of the electron mean free path.

The samples analyzed by EXAFS, were embedded under an inert atmosphere in a mixture (50 wt % each) of reagent grade octacosane and hexatriacontane and then pressed into wafers of uniform 10-mm thickness inside aluminum cells. Following this, 25-μm-thick Kapton windows were affixed using high-vacuum grade epoxy resin. The amount of material embedded in each cell was chosen so as to give a total X-ray absorption of about 1.5 at the Mo K edge.

X-ray absorption data were collected at the National Synchrotron Light Source (Brookhaven National Laboratory, Upton, NY) on beamline X-11A. The data were obtained in transmission mode, using a pair of GSK Scientific ionization detectors filled with krypton (sealed, post sample detector) and flowing argon (pre sample detector), respectively, both at atmospheric pressure. All samples were cooled to about 100 K before spectra were taken. For all samples and the reference (bulk crystalline $Mo(CO)_6$, in which the Mo–C distance determined by crystallography[10] is 2.065 Å), the Mo K edge at 20.000 keV was scanned beginning at 200 eV before, and ending at about 1300 eV above the edge. The monochromator energy origin was calibrated using a 5-μm molybdenum foil.

Normalization of the X-ray absorption data to the edge height and extraction and k weighting of the EXAFS $\chi(k)$ function were performed according to standard methods.[11,12] Before transforming the X-ray absorption data to momentum space, the absorption threshold was calibrated by linear extrapolation of the preedge (−200 to −30 eV) and postedge (50 to 200 eV) regions across the edge, then selecting the datapoint midway between these lines, and setting its abscissa to zero energy. Next, a linear baseline was calculated by fitting the region from about 100 eV above the edge to the end of the data set; this was subtracted from the data. Following this, the data were truncated to include the range containing the EXAFS information (15–1275 eV above the edge). After transforming into k space (k^1 weighted) and dividing by the height of the absorption edge, a cubic spline fit was applied as a further correction for low-frequency oscillations in the background. The data were next Fourier transformed over the range 3.3–16.2 Å^{-1}.

Isolation of the EXAFS due to photoelectron back-scattering from selected coordination shells was accomplished by the technique of Fourier filtering[11,12] and back-transforming into k space. In all cases, a symmetric Hanning apodization function (with a rectangular section 70% of the total width) was used as the filtering window. The overall window width was chosen to be 1.1 Å in all cases.

Determination of the structural parameters (interatomic distances, coordination numbers, static disorder and inner potential) of the samples, was made by simultaneous least-squares fitting of each filtered, back-transformed data set using phase and amplitude functions extracted from the reference compound.

Results and Discussion

Precursor $n[Mo(CO)_6]$–$Na_{56}Y$. In this section we very briefly recall some old data[2–4] and present some new information for $n[Mo(CO)_6]$–$Na_{56}Y$ which is relevant to the novel $n[MoO_x]$–$Na_{56}Y$ product phases.

(5) Dwyer, J.; Dyer, A. *Chem. Ind.* **1984**, *237* and references therein.
(6) Ozin, G. A.; Godber, J. *J. Phys. Chem.* **1988**, *92*, 4980.
(7) Swift, P. *Surf. Interfac. Anal.* **1982**, *4*, 47; ASTM Standard E 105, Vol. 03.06, 1984.
(8) Bryson, C. E. *Surf. Sci.* **1987**, *189/190*, 50.
(9) Scofield, J. H., *J. Electron. Spectrosc.* **1976**, *8*, 129.
(10) Arnesen, S. P.; Seip, H. M. *Acta. Chem. Scand.* **1966**, *20*, 2711.
(11) Sayers, D. E.; Bunker, B. A. *X-ray Absorption: Principles, Applications, Techniques of EXAFS, SEXAFS and XANES*; Koningsberger, D. C., Prins, R., Eds.; Wiley: New York, 1988; Chemical Analysis Vol. 92.
(12) Lee, P. A.; Citrin, P. H.; Eisenberger, P.; Kincaid, B. M. *Rev. Mod. Phys.* **1981**, *53* (4), 769.
(13) Anderson, S. L. T.; Howe, R. F. *J. Phys. Chem.* **1989**, *93*, 4913.
(14) Wagner, C. D.; Riggs, W. M.; Davis, L. E.; Moulder, J. F.; Muilenberg, G. E. *Handbook of X-Ray Photoelectron Spectroscopy*; Perkin-Elmer: Eden Prairie, MN, 1979.
(15) Swartz, W. E. Jr.; Hercules, D. M. *Anal. Chem.* **1971**, *43* (13), 1774.

Table I. Mo($3d_{5/2}$) Binding Energies for $Mo(CO)_6$, MoO_3, and MoO_2 in Various Media (Numbers in Parentheses Indicate Literature References)

sample	bulk	in zeolite Y
$Mo(CO)_6$	226.6[15]	227.8[13]
MoO_2	229.4[14]	231.7
MoO_3	232.6[14]	233.6

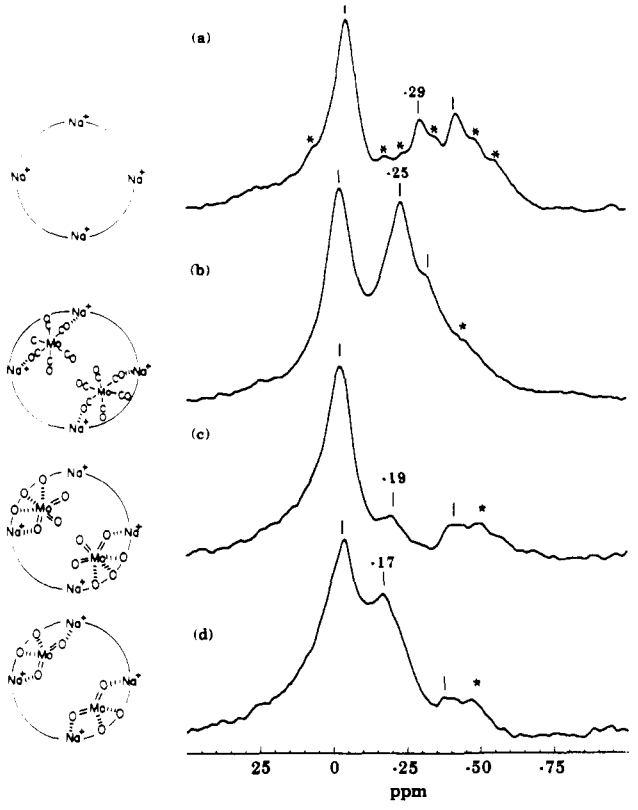

Figure 2. ^{23}Na DOR NMR spectra of (a) dehydrated $Na_{56}Y$, (b) $16[Mo(CO)_6]$–$Na_{56}Y$, (c) $16[MoO_3]$–$Na_{56}Y$ and (d) $16[MoO_2]$–$Na_{56}Y$. The asterisks indicate spinning sidebands.

Vapor-phase impregnation of $Mo(CO)_6$ into vacuum thermally dehydrated $Na_{56}Y$ yields α-cage encapsulated $n[Mo(CO)_6]$–$Na_{56}Y$. Quantitative gravimetry shows that saturation adsorption corresponds to $n = 16$, which represents $2[Mo(CO)_6]$–$Na_{56}Y$ per α-cage. Powder XRD of $n[Mo(CO)_6]$–$Na_{56}Y$ demonstrates that the degree of crystallinity and the lattice integrity of the host $Na_{56}Y$ remain intact, with the unit cell size (24.69 Å) essentially unaffected by the presence of the guest $Mo(CO)_6$ over the full loading range. No evidence for bulk $Mo(CO)_6$ could be found in these samples, which is consistent with complete internal, rather than external confinement of $Mo(CO)_6$ in $Na_{56}Y$. Supporting evidence for this proposal can be found in the XPS of $n[Mo(CO)_6]$–$Na_{56}Y$ which show no evidence for surface enrichment (bulk versus surface elemental analysis for Na:Si:Al:Mo ratios). The $Mo(3d_{5/2})$ core level binding energy of $n[Mo(CO)_6]$–$Na_{56}Y$ was measured at 227.8 eV, which when compared to the value (Table I) of 226.6 eV for solid $Mo(CO)_6$ indicates a 1.2-eV upward shift. This shift to higher energy implies some degree of charge transfer from the $Mo(CO)_6$ guest to the $Na_{56}Y$ host which can be attributed to anchoring rather than to a formal oxidation process.

The single T_{1u} IR-active ν_{CO} stretching mode (1984.4 cm^{-1}, *n*-hexane) of regular O_h symmetry $Mo(CO)_6$, is split into six resolved bands[3] in $n[Mo(CO)_6]$–$Na_{56}Y$. Only the highest frequency (normally Raman active) component of the ν_{CO} sextet is depicted in Figure 4. The frequency and intensity pattern of this ν_{CO} sextet provide compelling

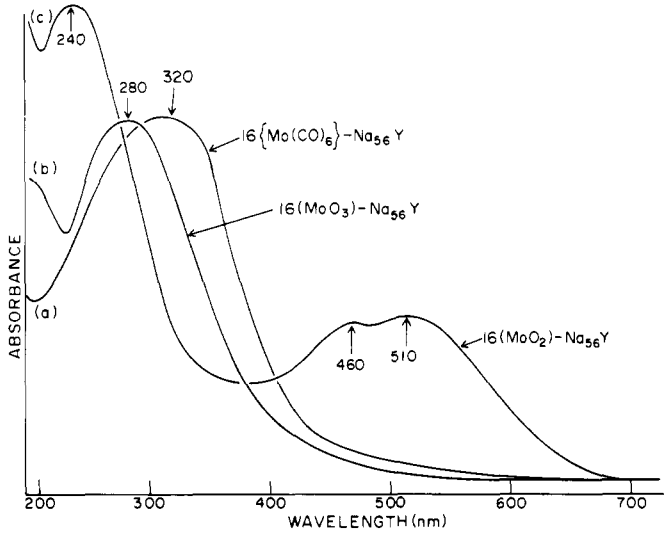

Figure 3. UV–visible optical spectra of (a) $16[Mo(CO)_6]$–$Na_{56}Y$, (b) $16[MoO_3]$–$Na_{56}Y$, and (c) $16[MoO_2]$–$Na_{56}Y$.

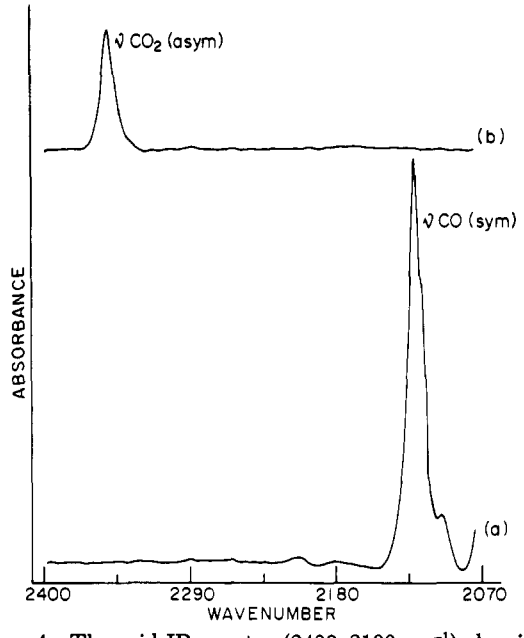

Figure 4. The mid-IR spectra (2400–2100 cm^{-1}) showing the photooxidation of α-cage encapsulated $Mo(CO)_6$ in the presence of oxygen: (a) $16[Mo(CO)_6]$–$Na_{56}Y$ and (b) the sample (a) after 1 h photooxidation.

evidence for a C_{2v} or lower symmetry *trans*-(ZONa)···(OC)$Mo(CO)_4$(CO)···(NaOZ) anchoring geometry for the host–guest complex. Site-selective, adsorption-induced far-IR cation translatory mode frequency shifts, together with ^{23}Na MAS and DOR NMR chemical shifts[16] and intensity alterations (Figure 2) all support the proposal of ZONa···OC anchoring interactions between site II Na^+ cations and the oxygen end of two *trans*-carbonyl ligands of the $Mo(CO)_6$ guest.

EXAFS spectroscopy was applied to a series of related samples, in which the host was $Rb_{56}Y$, in order to take advantage of structural information available through analysis of both the Mo–K and Rb–K X-ray absorption edges. The analysis of the structure of $8[Mo(CO)_6]$–$Rb_{56}Y$ confirms that the integrity of the $Mo(CO)_6$ guest is maintained following encapsulation in $Rb_{56}Y$, with minimal

(16) Jelinek, R.; Özkar, S.; Ozin, G. A. *J. Phys. Chem.* **1992**, *96*, 5949. Jelinek, R., Malek, A., Ozin, G. A., Özkar, S., Pastore, H. O. *J. Am. Chem. Soc.*, in press.

perturbation of the Mo–C–O and Mo–C–O bond lengths and coordination numbers.[3] Some support for ZORb···OC interactions is found from the small changes observed in the oxygen coordination number around a Rb^+ cation on passing from $Rb_{56}Y$ to $8[Mo(CO)_6]$–$Rb_{56}Y$. However, since only 16 out of 56 Rb^+ cations are affected by this anchoring interaction and since coordination numbers determined by the analysis of EXAFS data are usually accurate only to within about 20%, such evidence for cation–carbonyl binding is considered equivocal. A recent quantitative kinetic study[17] of the dissociative substitution reaction of ^{12}CO in $n[Mo(CO)_6]$–$M_{56}Y$ (where M = Li, Na, K, Rb, Cs; $0 < n \leq 16$) by ^{13}CO and $P(CH_3)_3$ dramatically confirms the existence and importance of ZOM···OC interactions. The activation parameters vary systemically with the number, ionic potential and spatial demands of the α-cage site II, III cations; in particular, they are substantially modified relative to the corresponding systems in the gas and liquid phases.

Of relevance to the photooxidation reaction of $n[Mo(CO)_6]$–$Na_{56}Y$ by O_2, is the UV–visible reflectance spectrum of this precursor shown in Figure 3. The intense broad absorption centered around 320 nm is assigned to the Mo(4d) → CO(π^*) MLCT excitation. This spectral feature is essentially the same as that found for $Mo(CO)_6$ in solution, and turns out to be the "photoactive state" responsible for the intrazeolite transformation of $n[Mo(CO)_6]$–$Na_{56}Y$ to $n[MoO_3]$–$Na_{56}Y$ (which is described in the following section). Optical shifts (comparing zeolite encapsulated with solution phase $Mo(CO)_6$) which would be anticipated on the basis of the 1.2 eV shift observed in the XPS spectra, are likely obscured by the breadth of the optical absorption.

Photooxidation Product $n[MoO_3]$–$Na_{56}Y$. A combination of quantitative in situ mid-IR spectroscopy and gravimetry shows that the photoinduced oxidation of $n[Mo(CO)_6]$–$Na_{56}Y$, at room temperature in 600 Torr of O_2, proceeds according to the following scheme:

$$n[Mo(CO)_6]\text{–}Na_{56}Y + {}^9/_2 nO_2 \xrightarrow{h\nu} n[MoO_3]\text{–}Na_{56}Y + 6nCO_2$$

over the entire loading range of $0 < n \leq 16$ (Figure 4). This reaction does not occur in the dark. The Mo:O stoichiometry of the product is found to be 1:3 (quantitative gravimetry) and six "intrazeolite" CO_2 molecules (quantitative mid-IR spectroscopy) are produced for every $Mo(CO)_6$ guest. There is no evidence for the cogeneration of measurable amounts of CO either within the zeolite or in the gas phase. Powder XRD of $n[MoO_3]$–$Na_{56}Y$ shows that the degree of crystallinity and the lattice integrity of the host $Na_{56}Y$ are maintained, with the unit cell size (24.69 Å) essentially unaltered by the presence of the MoO_3 guest over the full loading range. No evidence for bulk MoO_3 could be found from PXRD, which is consistent with the formation of internally confined MoO_3 guests in $Na_{56}Y$. This proposal finds convincing support in the XPS of $n[MoO_3]$–$Na_{56}Y$ (Figure 5), which shows no evidence for surface enrichment (bulk versus surface elemental analysis, Na:Si:Al:Mo ratios) and moreover, a 5.8-eV shift to a higher value of the $Mo(3d_{5/2})$ binding energy (233.6 eV) relative to that (227.8 eV) of the zerovalent precursor $n[Mo(CO)_6]$–$Na_{56}Y$. The $Mo(3d_{5/2})$ binding energies[13,15] for bulk MoO_3 and bulk $Mo(CO)_6$ are 232.7 and 226.6 eV, respectively (Table I). These results are consistent with the photooxidation product being zeolite Y encapsulated molybdenum(VI) oxide. The fwhm peak widths of ca. 2 eV which were observed for the zeolite encapsulated species are larger than those observed[13] for single valence state bulk species such as $Mo(CO)_6$ and MoO_3. This likely reflects the concept that the MoO_3 monomers in zeolite Y are anchored at some distribution of both site II and site III locations (offering slightly different electronic environments), rather than being a mixed distribution of, for example, MoO_3 and MoO_2 oxide moieties. In the case of mild (25 °C) air oxidation[13] of a $Mo(CO)_6$–$Na_{56}Y$ sample in which mixed valence states were observed, the XPS spectrum showed a greater number of peaks which were well separated. XPS peaks[15] comparing Mo(IV) with Mo(VI) are separated by about 3 eV.

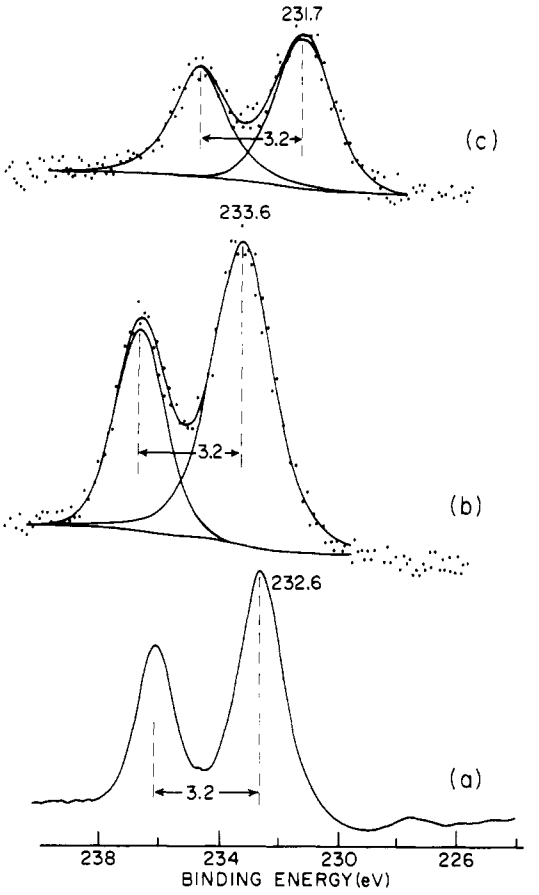

Figure 5. High-resolution XPS spectra for the Mo(3d) region: (a) bulk MoO_3, (b) $16[MoO_3]$–$Na_{56}Y$ and (c) $16[MoO_2]$–$Na_{56}Y$.

The XPS probe also proves to be of some value in clarifying the fate of the carbonyl ligands during the process of photooxidizing $n[Mo(CO)_6]$–$Na_{56}Y$ to $n[MoO_3]$–$Na_{56}Y$. In situ mid-IR monitoring of the photoannihilation of the $Mo(CO)_6$ guest in the presence of 600 torr of O_2 shows a well-behaved one-to-one correspondence with the growth of intrazeolite CO_2 (the experimental method and full data for the comparable $W(CO)_6$ system are presented elsewhere[2]). In mechanistic terms, the lack of observed CO implies an oxidation process which involves the transformation of either ligated or free CO groups to CO_2, by either gaseous O_2, coordinated O_2, or oxometal groups. It is clear that further quantitative studies, employing comprehensive carbon and oxygen isotope labelling experiments, will be required in order to elucidate more details of this mechanism. There are however some clues concerning the above ideas which are already available from an examination of the C(1s) binding energies in the XPS spectra of $Na_{56}Y$ and $n[Mo(CO)_6]$–$Na_{56}Y$ (Figure 6).

(17) Ozin, G. A.; Özkar, S.; Pastore, H. O.; Poë, A. J.; Vichi, E. J. S. *J. Chem. Soc., Chem. Commun.* **1991**, 141; *ACS Symp. Ser.* **1992**, *499*, 314. Ozin, G. A., Poë, A. J., Pastore, H. O. *J. Am. Chem. Soc.*, in press.

Table II. Structural Parameters Determined by Analysis of Mo-K EXAFS Data

sample	atom pair	coordination no.	bond dist. (Å)	static disorder (Å^2)	inner potential (eV)
16[MoO_3]-$Na_{56}Y$	Mo–O	3.25	1.73	0.0000	1.5
	Mo–O	2.77	1.88	0.0019	1.6
16[MoO_2]-$Na_{56}Y$	Mo–O	5.08	1.80	0.0024	0.6

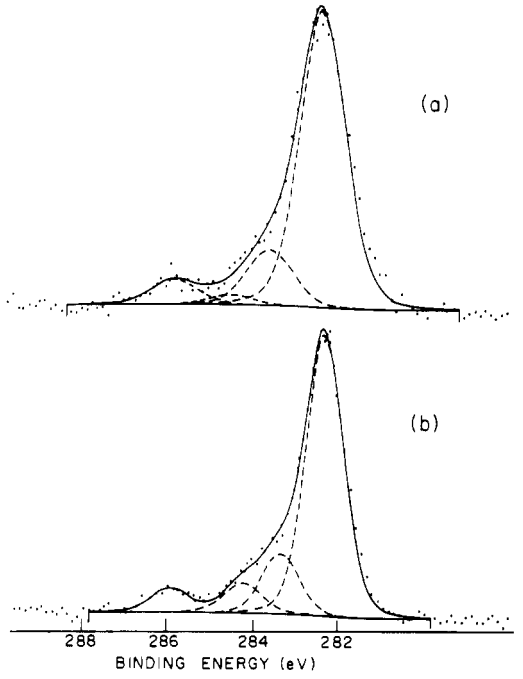

Figure 6. High-resolution XPS spectra for the C(1s) region: (a) virgin dehydrated $Na_{56}Y$; (b) 16[MoO_3]-$Na_{56}Y$.

In the virgin dehydrated $Na_{56}Y$ host, the usual pattern of C(1s) binding energies is displayed, which arises from the adventitious carbon component (trace hydrocarbon surface contaminants which are always present in these materials[18]). Within the carbon detection limit capability of XPS (ca. 1000 ppm), there is essentially no change in the C(1s) signal intensity or line shape throughout the impregnation and photooxidation sequence of steps. This observation implies that C deposition and CO_2 formation do not occur through for example, the Boudart disproportionation reaction:[19] $2CO \rightarrow CO_2 + C$, which might have been thermally or photolytically induced by the zeolite itself or by molybdenum carbonyl, oxide, or metallic reaction intermediates. Furthermore, if the above reaction were the source of the CO_2, the graphite deposition would amount to 7.6 wt % for 32[$Mo(CO)_6$]-$Na_{56}Y$ and would have been easily detectable by XPS. Control experiments involving thermal and photolytic treatments of CO, O_2 and mixtures thereof exposed to virgin $Na_{56}Y$ clearly demonstrate that this is not the source of the observed CO_2 in the photooxidation of n[$Mo(CO)_6$]-$Na_{56}Y$.

Results of the analysis of the Mo K-edge EXAFS data are shown in Figure 7 and in Table II. The reference phase and amplitude functions which were used in the curve-fitting procedure for the Mo–O atom pair were taken from the Mo–C shell of bulk $Mo(CO)_6$. This makes use of the assumption of chemical transferability of these functions, which is acceptable[12] for light back-scatterers differing in atomic number by 1. The Mo–C–O second shell was rejected because of the dissimilarity in distance (in the oxide samples versus the bulk carbonyl), and the near linearity of the Mo–C–O angle, which would cause the

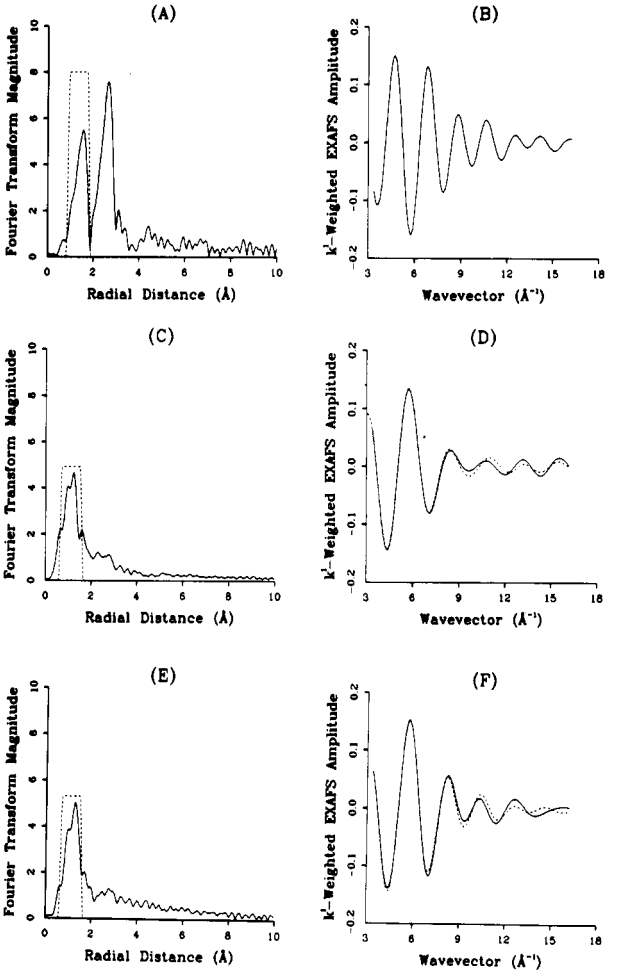

Figure 7. Results of the analysis of Mo K-edge EXAFS data: (A) Fourier transform magnitude for bulk $Mo(CO)_6$, dashed curve shows window used for inverse transformation; (B) inverse Fourier transform of filtered data in (A); (C) Fourier transform magnitude for 16[MoO_3]-$Na_{56}Y$; (D) inverse Fourier transform of filtered data in (C), dashed curve indicates results of fit using standard methods[11,12] and data from reference compound EXAFS; (E) Fourier transform magnitude for 16[MoO_2]-$Na_{56}Y$; (F) inverse Fourier transform of filtered data in (E), dashed curve indicates results of fit and data from reference compound EXAFS.

amplitude of the corresponding EXAFS to be enhanced through the phenomenon[20] of forward scattering by the intervening C atom. Probably the most interesting feature of the Fourier transform magnitude plot for the 16-[MoO_3]-$Na_{56}Y$ sample is the lack of peaks at apparent radial distances greater than about 2 Å. Unlike the various tungsten oxide materials reported elsewhere,[2-4] in which dimers were detected by the presence of a W–W "second shell" scattering contribution in the EXAFS, the molybdenum EXAFS gave no evidence of this, even when k^3 weighting was used as a means of emphasizing any such features. The back-transformed k^1-weighted data (delimited by the Fourier filtering window also shown in Figure 7) were fit according to a model having two "shells" of oxygen atoms. Coordination numbers were determined to

(18) Barr, T. L.; Chen, L. M.; Mohsenian, M.; Lishka, M. A. *J. Am. Chem. Soc.* **1988**, *110*, 7962 and references therein.
(19) Ichikawa, S.; Poppa, H.; Boudart, M. *J. Catal.* **1985**, *91*, 1.
(20) Cramer, S. P.; Hodgson, K. O.; Stiefel, E. I.; Newton, W. E. *J. Am. Chem. Soc.* **1978**, *100* (9), 2748.

Scheme I

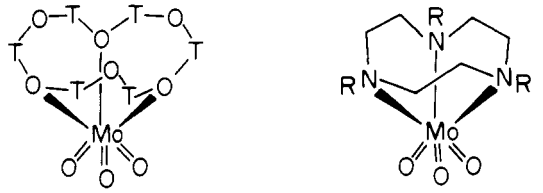

(I) (II)

be 3.25 oxygen atoms at a distance of 1.73 Å and 2.77 oxygen atoms at a distance of 1.88 Å. A structural model which is consistent with these observations is that of a monomeric *fac*-MoO_3 moiety (with three shorter Mo=O bonds) stabilized through coordination to the three framework oxygen atoms (longer Mo–O bonds) of a six-ring lattice site. It would also be reasonable to assign the anchored moiety to a four-ring site (having only two long Mo–O bonds), since the accuracy with which the curve-fitting procedure can determine coordination numbers is normally about ±1 atom under these circumstances. The "zeolate" ligating properties[21] of this monomeric *fac*-trioxomolybdenum(VI) unit (I) in Scheme I find remarkable molecular analogs in $LMoO_3$ complexes[22] (II) in Scheme I, where L represents for example, 1,4,7-triazocyclononane or *N,N',N''*-trimethyl-1,4,7-triazocyclononane. It is significant that these two complexes are essentially quantitatively formed by the oxidative decarbonylation of $LMo(CO)_3$ by 30% H_2O_2 in THF at 45 °C.

As mentioned earlier for $n[Mo(CO)_6]$–$Na_{56}Y$, ^{23}Na MAS and DOR NMR spectra clearly depict site II Na^+ cation adsorption-induced chemical shifts[16] and intensity alterations (Figure 2). Observations of this kind demonstrate the presence of Na^+ cation based anchoring interactions. Similar effects are observed for the site II Na^+ cations in the photooxidation product $n[MoO_3]$–$Na_{56}Y$ (Figure 2). This strongly suggests that the oxygen atom of at least one of the terminal oxo-metal groups in the monomeric *fac*-trioxomolybdenum(VI) moiety may bind to the site II Na^+ cation, denoted (ZO)···MoO_3···(NaOZ). This proposal is also supported by comparison with the ligating properties of the MoO_3 moiety in $LMoO_3$ complexes toward cationic metal centers.[22] For instance, the reaction of $LMoO_3$ with $Co(ClO_4)_2 \cdot 6H_2O$ in dry methanol yields a blue solution from which crystals of the composition $[(LMoO_3)_4Co](ClO_4)_2$ precipitate, whereas the same reaction carried in aqueous solution produces a pink solution containing $[Co(H_2O)_6]^{2+}$. This indicates that the oxygen atoms of the $LMoO_3$ units are weaker donor ligands than water but stronger than methanol.[22] It is believed that the central Co(II) ion is tetrahedrally surrounded by four oxygen atoms, one from each $LMoO_3$ unit, which function as monodentate neutral ligands. The analogy between (ZO)···MoO_3···(NaOZ) and (L)···MoO_3···(Co) therefore becomes clear, bringing forth the idea of the zeolite cavity acting as a macrospheroidal multidentate multisite ligand ("zeolate") towards various guests,[17,21] in this particular case a *fac*-trioxomolybdenum(VI) unit. In this context, it is worth noting that the almost 1-eV upward shift in the $Mo(3d_{5/2})$ binding energy observed on passing from bulk MoO_3 (the stable form has a complex layered structure with each Mo^{6+} center surrounded by a distorted octahedron of oxygen atoms) to $n[MoO_3]$–$Na_{56}Y$ (Table I) could arise from initial (Koopman) and final (relaxation) state effects. These relate to the change from a delocalized band-type situation in bulk MoO_3 to a more localized molecular orbital type scheme in (ZO)···MoO_3···(NaOZ). Here one expects higher ionization potentials as a consequence of lower valence electron charge and lower coordination number (initial state effect) and lower valence electron screening (final state effect) of molecular relative to bulk MoO_3. It is likely however that sodium cation/oxomolybdenum bond interactions also contribute to this upward binding energy shift, in a manner similar to that observed on comparing the precursor $n[Mo(CO)_6]$–$Na_{56}Y$ to bulk $Mo(CO)_6$, as described earlier (Table I).

On the basis of the proposed structural model for $n[MoO_3]$–$Na_{56}Y$, the broad, intense UV absorption band centered around 280 nm can be assigned to $O^{2-}(2p\pi) \rightarrow Mo^{6+}(4d)$ LMCT excitations (Figure 3). This assignment is consistent with those proposed[23] for Mo^{6+} complexes having comparable coordination environments. The LMCT region shows a tendency to broaden and red shift with increasing loading over the range $0 < n \leq 16$. This is most likely indicative of through bond and/or through space intra- and/or intercavity coupling between *fac*-trioxomolybdenum(VI) moieties.

Thermal Vacuum Reduction Product $n[MoO_2]$–$Na_{56}Y$. Quantitative gravimetry experiments demonstrate that a 400 °C thermal vacuum treatment of white samples of $n[MoO_3]$–$Na_{56}Y$ proceeds smoothly according to the following reaction scheme:

$$n[MoO_3]\text{–}Na_{56}Y \underset{400\ °C}{\overset{400\ °C,\ \text{vacuum}}{\rightleftharpoons}} n[MoO_2]\text{–}Na_{56}Y + \tfrac{1}{2}nO_2$$

to produce "puce" colored samples of $n[MoO_2]$–$Na_{56}Y$ over the entire loading range of $0 < n \leq 16$. This reduction process can be quantitatively reversed by exposing the sample to O_2 at 400 °C. PXRD shows that there is no change in the degree of crystallinity or lattice integrity of the $n[MoO_3]$–$Na_{56}Y$ and $n[MoO_2]$–$Na_{56}Y$ materials relative to the original $Na_{56}Y$ host, even upon cycling the above redox process many times; the unit cell size for all of the materials remains constant at around 24.69 Å over the entire loading range $0 < n \leq 16$. No evidence for bulk MoO_2 (distorted rutile type structure with Mo–Mo distances of 2.51 Å) could be found from PXRD or EXAFS, which is consistent with the creation of strictly internally confined MoO_2 units in $Na_{56}Y$. As observed for the photooxidation product $n[MoO_3]$–$Na_{56}Y$, there is no XPS evidence of surface enrichment in $n[MoO_2]$–$Na_{56}Y$, thus giving further support for the proposal of internal confinement. Of particular significance is the observation that the $Mo(3d_{5/2})$ binding energy in $n[MoO_2]$–$Na_{56}Y$ was 1.9 eV lower than that in $n[MoO_3]$–$Na_{56}Y$ (Table I). With a shift of approximately 1 eV per formal oxidation state, these observations provide strong support for the aforementioned two-electron reduction process between oxomolybdenum(VI) and oxomolybdenum(IV) centers and is fully consistent with the thermal reduction product being zeolite Y encapsulated molybdenum(IV) oxide. As with the Mo(VI) photooxidation product, the observed fwhm peak widths suggest a distribution among anchoring sites II and III of single valence state MoO_2 monomers.

Results of the analysis of EXAFS data for the thermal vacuum reduction product $n[MoO_2]$–$Na_{56}Y$ are presented in Figure 7 and Table II. As was the case for the zeolite Y encapsulated molybdenum(VI) material, no evidence for Mo–Mo back-scattering was found, hence leading to the proposal that dimeric oxide species are not formed (even when k^3 weighting of the data was performed in an attempt

(21) Ozin, G. A.; Özkar, S. *Chem. Mater.* **1992**, *4*, 511. Bowes, C. L., Ozin, G. A., Steele, M., *MRS Symp. Ser.* **1992**, *277*, 105.
(22) Roy, P. S.; Wieghardt, K. *Inorg. Chem.* **1987**, *26*, 1885.
(23) Iwasawa, Y.; Sato, Y., Kuroda, H. *J. Catal.* **1983**, *82*, 289 and references therein.

Scheme II

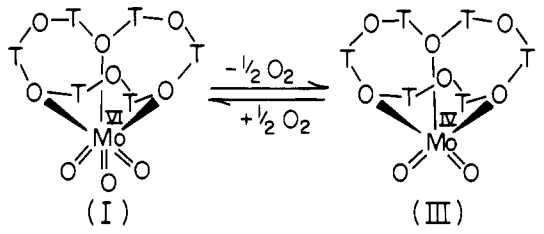

(I) (III)

to emphasize any such features). The back-transformed k^1-weighted data (delimited by the Fourier filtering window also shown in Figure 7) were best fit according to a model having a shell of oxygen atoms at only a single distance. The coordination number was determined to be 5.08 with a distance of 1.80 Å. Much like the case of the $16[MoO_3]$–$Na_{56}Y$ material, a structural model which is consistent with these observations is that of a monomeric *cis*-MoO_2 moiety anchored by three O atoms in a zeolite six ring site (or conceivably the two O atoms of a four-ring site). It is thus likely that the reduction process involves the removal of one of the "short-bond" oxygens in the anchored MoO_3 entity, and a readjustment of the position of the molybdenum atom such that all five oxygen atoms become essentially equidistant from the molybdenum center. The bond length is observed to be longer than in the case of the Mo^{6+} moiety, which is expected for a reduction to Mo^{4+}, and interestingly is the arithmetic average of the "short" and "long" distances determined from the $16[MoO_3]$–$Na_{56}Y$ EXAFS data. The "zeolate" ligating properties of the monomeric *cis*-MoO_2 moiety (III) bear a strong resemblance to those of its redox active partner (I) *fac*-MoO_3, as shown in the aesthetically satisfying relationship[17,21] between the redox interconvertible pair illustrated in Scheme II.

Once again, ^{23}Na MAS DOR NMR provides insight about the "secondary" anchoring interactions between the MoO_2 moiety and the α-cage Na^+ cations. Figure 2 clearly demonstrates evidence for site II Na^+ cation adsorption induced chemical shifts and intensity alterations for $n[MoO_2]$–$Na_{56}Y$, which closely parallel those observed for $n[MoO_3]$–$Na_{56}Y$. Both of these zeolite Y encapsulated monomers tend to participate in secondary anchoring interactions which involve at least one of their terminal oxometal groups and site II Na^+ cations and are denoted (ZO)···MoO_3···(NaOZ) and (ZO)···MoO_2···(NaOZ).

Given the proposed structural model for $n[MoO_2]$–$Na_{56}Y$, one can assign the intense broad UV absorption band centered near 240 nm to $O^{2-}(2p\pi) \rightarrow Mo^{4+}(4d)$ LMCT excitations. The EPR silence of this species, along with the observed ^{23}Na MAS and DOR NMR activity, imply that the electronic ground-state configuration of the Mo^{4+}, center is most likely diamagnetic spin-paired d^2. The intense visible absorptions (responsible for the puce color) centered around 460 and 510 nm are best assigned to 4d–4d ligand field transitions. These band assignments are consistent with those proposed for other Mo^{4+} complexes having comparable coordination environments.[24] The UV and visible absorptions show a tendency to broaden and red shift with increasing loading over the range $0 < n \leq 16$, (as observed earlier for $n[MoO_3]$–$Na_{56}Y$) and are probably indicative of either through bond and/or through space intra- and/or intercavity coupling between the *cis*-dioxomolybdenum(IV) units.

All of these structural proposals for the molybdenum system are conveniently summarized in Figure 1 and are presented in a similar form to those used for the related tungsten system,[2-4] in order to highlight the similarities and differences between the two systems.

Conclusions

In Figure 1 an illustration of the relationship between the $n[M(CO)_6]$–$Na_{56}Y$ precursor and redox interconvertible $n[MO_{3-x}]$–$Na_{56}Y$ products is presented for both M = Mo and W, in order to outline the structural, anchoring, chemical and electronic similarities and differences between the two systems.

Some interesting and potentially useful features of this kind of "intrazeolite topotaxy" include the following:

(A) The ability to produce zeolite encapsulated "molecular metal oxides" under relatively *mild* conditions in a clean and quantitative fashion;

(B) The anchoring of well-defined monomeric, dimeric, and tetrameric oxometal units with "tunable" oxidation states, to specific extraframework cation sites, and distributions of site II and site III oxygen framework locations;

(C) Recognition of the concept of the "zeolate ligand"[17,21] (a collection of interconnected four- and six-ring aluminosilicate units, resembling macrocyclic crown ethers and which form a macrospheroidal multidentate multisite rigid "cavitate") having the ability to complex (stabilize) monomeric MO_3 and MO_2 moieties in much the same way as found in the coordination chemistry[22] of known *fac*-trioxometal (LMO_3) and cis-dioxometal (LMO_2) units;

(D) Discovery of thermally interconvertible redox active "zeolate complexes" which can be considered to be the molecular versions of bulk MO_{3-x}, nonstoichiometric crystallographic shear phases.

(E) Success in overcoming the usual difficulty in engineering well-defined oxometal site distributions on various substrates of interest in catalytic, solid-state, and materials chemistry, hence suggesting potentially valuable applications such as size and shape selective catalysis, chemoselective oxygen/oxidation sensors, molecule discriminating nanoelectronic and nonlinear optical devices (which could exploit the advantages of "quantum confinement" of metal oxide units which are semiconductors in their bulk form).

When evaluating the common threads and surprising differences to be found in the photooxidation chemistry of the precursor $n[M(CO)_6]$–$Na_{56}Y$ and the thermal reversible redox chemistry of the product $n[MO_3]$–$Na_{56}Y$ for M = Mo, W summarized in Figure 1, some of the key points which emerge and need addressing include the following:

(F) The only apparently isostructural pair in this group of "zeolate"-stabilized molecular metal oxides comprises the monomeric *cis*-dioxometal(IV) units. EXAFS structure analysis indicates that they (both MoO_2 and WO_2) reside on the oxygen six-ring and/or four-ring sites, and NMR results indicate the participation of secondary interactions between Na^+ cations and the oxygen end of an oxometal bond. Electronically they both appear to be diamagnetic with spin-paired d^2 ground states. The visible 4d–4d ligand field absorption responsible for the puce color of the (ZO)···MoO_2···(NaOZ) moiety undergoes the expected blue shift into the near UV (on changing to 5d–5d electronic excitations) to yield the pale yellow (ZO)···WO_2···(NaOZ) unit. With a judicious choice of zeolite host, one can easily envision how the 400 °C interconvertible redox pair:

$$(ZO)\cdots MoO_3\cdots(NaOZ) \rightleftarrows (ZO)\cdots MoO_2\cdots(NaOZ)$$

could for example be tailored as an oxygen and/or oxidation-state-selective chemical sensor, an information storage material, a smart window/display/mirror, or a

(24) Lever, A. B. P. *Inorganic Electronic Spectroscopy*, 2nd. ed.; Elsevier: Amsterdam, 1984.

selective hydrocarbon oxidation catalyst.

(G) One learns from the coordination chemistry[22] of *fac*-LMO_3 complexes of M = Mo, W that the propensity[21] of "zeolate"-ligated MO_3 to form dimeric units in the case of M = W^{6+} and monomeric units in the case of M = Mo^{6+} could be related to the anticipated greater intrinsic lability (reactivity) of the W^{6+} relative to the Mo^{6+} monomeric (ZO)···MO_3···(NaOZ) coordination sites. In this way, one can satisfactorily rationalize the following:

(i) The formation of dimeric (ZONa)···$O_2W(\mu\text{-}O)_2WO_2$···(NaOZ) from *trans*-(ZONa)···(OC)$W(CO)_4$-(CO)···(NaOZ) yet monomeric (ZO)···MoO_3···(NaOZ) from *trans*-(ZONa)···(OC)$Mo(CO)_4$(CO)···(NaOZ);

(ii) The thermal oxidation of monomeric (ZO)···WO_2···(NaOZ) to dimeric (ZONa)···$O_2W(\mu\text{-}O)_2WO_2$···(NaOZ) yet monomeric (ZO)···MoO_2···(NaOZ) to monomeric (ZO)···MoO_3···(NaOZ);

(iii) The formation of dimeric (ZONa)···$O_2W(\mu\text{-}O)$-WO_2···(NaOZ) from dimeric (ZONa)···$O_2W(\mu\text{-}O)_2WO_2$···(NaOZ), yet the nonexistence of Mo^{5+}–Mo^{5+}, or Mo^{6+}–Mo^{6+} analogs.

Acknowledgment. Funding for this project was provided by the Natural Sciences and Engineering Research Council of Canada's Operating and Strategic Grants Programs. The EXAFS research was carried at the National Synchrotron Light Source, Brookhaven National Laboratory, which is supported by the United States Department of Energy (Divisions of Materials Sciences and Chemical Sciences). Professor Özkar expresses his gratitude to the Middle East Technical University, Ankara, for granting him an extended leave of absence to conduct his research at the University of Toronto.

Registry No. O_2, 7782-44-7; CO_2, 124-38-9.

Effect of Chain Length on the Conductivity of Polyacetylene. Potential Dependence of the Conductivity of a Series of Polyenes Prepared by a Living Polymerization Method

L. Y. Park, D. Ofer, T. J. Gardner, R. R. Schrock,* and M. S. Wrighton*

Department of Chemistry, 6-331, Massachusetts Institute of Technology, Cambridge, Massachusetts 02139

Received May 5, 1992. Revised Manuscript Received September 3, 1992

The controlled ring-opening metathesis polymerization of 7,8-bis(trifluoromethyl)tricyclo[4.2.2.$0^{2,5}$]-deca-3,7,9-triene has been employed to prepare soluble polymers of low polydispersity that are precursors to polyenes. Films of these precursor polymers have been cast from solution onto platinum microelectrode arrays and have been heated to form films of polyacetylene in the molecular weight range 400–6500. These films have been characterized by in situ measurements of conductivity as a function of electrochemical potential in liquid SO_2/electrolyte. The results show a steady increase in conductivity with average chain length for samples with chain lengths in the range 11–60 double bonds, above which conductivity levels off as chain length continues to increase. All samples exhibit a finite potential window of conductivity which increases in width in the range 11–60 double bonds and does not change further with increasing chain length.

Introduction

The dependence of conductivity upon conjugation length is an issue of fundamental importance in the study of conducting polymers.[1] There is a great deal of interest in determining the relationship between properties observed for short polyenes and those for polyacetylene, an "infinitely long" polyene. The relative importance of intra- and intermolecular mechanisms of charge transport in these materials has been the subject of some discussion.[2,3] Studies of the conductivity of discrete polyenes containing between one and six double bonds showed that they are poor conductors and that there is little improvement in conductivity over this range of conjugation lengths.[4] Some studies of polyacetylene have indicated a strong dependence of conductivity on molecular weight,[3,5] while others have indicated no such correlation.[6] However, these previous studies have been limited by the difficulties associated with preparing polyacetylene in a controlled fashion using classical catalyst systems. The conjugation length in highly conducting polyacetylene has been estimated to lie in the range 20–50 double bonds.[7-10]

(1) *Conjugated Polymers*; Brêdas, J. L., Silbey, R. J., Eds.; Kluwer: Boston, 1991.
(2) Havinga, E. E.; Van Horssen, L. W. *Synth. Met.* **1986**, *16*, 55.
(3) Yaniger, S. I.; Kletter, M. J.; MacDiarmid, A. G. *Polym. Prepr. (Am. Chem. Soc., Div. Polym. Chem.)* **1984**, *25*, 264.
(4) Spangler, C. W.; Hall, T. J.; Sapochak, L. S.; Liu, P.-K. *Polymer* **1989**, *30*, 1166.
(5) Soga, K.; Nakamaru, M. *J. Chem. Soc., Chem. Commun.* **1983**, 1495.
(6) Schen, M. A.; Karasz, F. E.; Chien, J. C. W. *Makromol. Chem., Rapid Commun.* **1984**, *5*, 217.
(7) Bott, D. C. In *Handbook of Conducting Polymers*; Skotheim, T. A., Ed.; Marcel Dekker: New York, 1986; Vol. 2.
(8) Kuzmany, H.; Knoll, P. *Mol. Cryst. Liq. Cryst.* **1985**, *117*, 385.
(9) Schaffer, H. E.; Chance, R. R.; Knoll, K.; Schrock, R. R.; Silbey, R. In *Conjugated Polymeric Materials: Opportunities in Electronics, Optoelectronics, and Molecular Electronics*; Brêdas, J.-L.; Chance, R. R., Eds.; Kluwer Academic Publishers: Dordrecht, 1989.
(10) Williams, K. P. J.; Gerrard, D. L.; Bott, D. C.; Chai, C. K. *Mol. Cryst. Liq. Cryst.* **1985**, *117*, 23.

0897-4756/92/2804-1388$03.00/0